Experimental Study of Tendon Failure Analysis for a TLP Floating Offshore Wind Turbine

Experimental Study of Tendon Failure Analysis for a TLP Floating Offshore Wind Turbine

Yajun Ren [a, b], Wei Shi [c, d, e] *, Vengatesan Venugopal [a], Lixian Zhang [c], Xin Li [f]

[a] Institute for Energy Systems, The University of Edinburgh, Edinburgh, EH8 3DW, UK

[b] China Renewable Energy and Engineering Institute, Beijing, China

[c] Deep Water Engineering Research Centre, Dalian University of Technology, China

[d] State Key Laboratory of Coastal and Offshore Engineering, Dalian University of Technology, Dalian, China

[e] Ningbo Institute, Dalian University of Technology, Ningbo, China

[f] Institute for Earthquake Engineering, Faculty of Infrastructure Engineering, Dalian University of Technology, Dalian, China

* Correspondence: weishi@dlut.edu.cn (W. Shi)

Abstract

This paper describes an experimental study conducted on a multi-column tension leg platform (TLP) floating offshore wind turbine (FOWT). A prototype model of the TLP FOWT supporting the NREL 5-MW wind turbine with a scale ratio of 1:50 is tested under various wind and wave conditions at the State Key Laboratory of Coastal and Offshore Engineering at Dalian University of Technology, China. This work has particularly focused on the tendon failure and its impact on the dynamic response of the FOWT. Free decay tests, regular wave tests, wind-wave combined tests and tendon failure tests are conducted using different environmental parameters.

The results suggest that natural periods, dynamic responses of the platform, and forces in the tendons satisfy the design requirements. The analysis indicates that the impact of tendon failure on the platform surge, heave and pitch responses are found to be insignificant. When one of the tendons is broken, the adjacent tendons experience a significant increase in tensile force; and, the maximum tensile force in the remaining tendon is found to increase by about

130%. The overstepping of the minimum breaking load as recommended by the design standard DNV GL is not reached, and this indicates that the safety of the system is ensured even during the harshest failure condition.

Key words: TLP; Floating wind; Tendon failure; Experimental analysis

1. Introduction

Offshore wind energy technologies have developed rapidly over the past decade. A total of 21.1 GW of new offshore wind capacity was connected to the grid around the world in 2021, which reached the highest in the offshore wind industry [1]. As conventional bottom-fixed offshore wind turbines are highly limited by water depth [2, 3], floating offshore wind turbine (FOWT) technologies have emerged as a solution for exploiting the enormous energy potential over the deep ocean and accelerating decarbonisation and energy transition [4]. Since the first floating offshore wind turbine, Hywind Demo was installed in 2007, the industry has advanced to a high 'technology readiness level'. A total of 23 floating wind projects were installed over the world within 5 years; e.g. Yinling Hao demonstration project in Guangdong, China in 2021; WindFloat Atlantic wind farm in Portugal in 2020; and Hywind Tampen floating wind farm planned in Norway by 2022 [5-8]. However, the floating wind turbines installed in deep ocean experience severe environment than those located near shore or onshore. The complex nature of wind, wave, current and their loadings acting on the FOWT structure raise difficulties in their design and analysis, limiting the development of the floating wind industry [9-11]. Thus, one of the most urgent tasks for increasing the reliability of the technology is to understand the dynamic characteristics of FOWTs under the stochastic environment.

For a FOWT, a floating platform is the key subsystem for retaining the whole structure afloat and stable. The hydrodynamic loading and resulting motion of the floater come from waves and currents and these can significantly influence the power performance by transferring the loads to the wind turbine. These loads include the contribution from viscous effect (drag loading), inertia (added mass), damping (radiation), buoyancy and mooring

(restoring), wave scattering (diffraction), sea currents and various nonlinear effects. The 6-DOF-motion responses of FOWT are coupled with the rotation of the wind turbine, making the dynamics of the floating wind turbine more complicated [12-15].

The substructure (i.e. the floating platform) of a FOWT design has normally been grouped into four main concepts; barge, semisubmersible, spar buoy and tension leg platform (TLP). TLPs have been widely utilised in the offshore oil and gas industry because of their high stability provided by the pretensioned tendons [16]. For floating offshore wind turbines, TLP can effectively reduce the structural loading on towers and blades and thus sustain safe turbine operation.

To date, several concepts of TLP FOWT have been proposed and investigated. PelaStar was designed by Glosten Associates Company. It has the advantages of a simple structure, minimal platform motions and low cost. Denis Matha [17] optimised the four-spoke TLP FOWT, which was initially designed by Withee [18]. The dynamic responses of the platform were calculated using the fully coupled time-domain aero-hydro-servo-elastic-mooring simulation tool, FAST [19] and compared with that of barge and spar buoy platforms. The results indicated that the TLP has the lowest responses in surge, sway, heave, roll and pitch, and, the fatigue lifetime of the TLP is longer than that of spar and barge. A multi-column TLP FOWT was proposed by Ding et al. [20] and this study showed the feasibility of wet towing utilising for TLP, which can effectively reduce the cost of transportation. A WindStar concept was introduced by Zhao et al [21]. The performance of the prototype was examined by both numerical modeling (by FAST) and tank testing [22], demonstrating the satisfying performance of TLP under various environmental conditions. Overall, these studies showed the feasibility and superiority of TLP technology in the application of the floating offshore wind industry.

Tank testing techniques have been well developed and seen as a valid approach in the research and design of FOWTs. The experiment on two types of TLP platforms was carried

out by Naqvi with a scale factor of 1:100 [23]. To focus on the hydrodynamics of the platform, the topside rotor of the turbine was substituted by a plastic drag disk to imitate the rotor thrust. This simplified approach was also adopted by several studies when the main scope of the test was to investigate the hydrodynamic performance of the floating platform. Wright et al. [24] carried out experimental testing of a TLP at scales of 1:50 and 1:30. The study aimed to investigate the effects of spring dampers on the dynamic response of tendons and platforms with respect to different test scales. The results demonstrated a reduction in tension loadings and an increase of platform dynamic responses with the utilisation of spring damper. A larger scale was recommended by the author as the results obtained with the smaller scaling ratio showed higher consistency in RAOs. Murfet and Abdussamie tested a 1:112 TLP FOWT model with non-rotating blades to examine the motion and tendon responses when subjected to combined wind and regular wave conditions [25]. In the model test carried out by Oguz, et al., the TLP model was incorporated with an electric ducted fan [26]; the instantaneous rotor thrust was modelled using a software-in-the-loop (SIL) approach to actively control the fan, which enabled coupling between the platform motion and aerodynamic loading.

As an important substructure of FOWT, the mooring system has been widely studied for a better understanding of its characteristics and improving the modelling and design techniques. The basics of mooring cable analysis were comprehensively reviewed and discussed by Giuseppe in [27, 28]. The modelling approaches of mooring systems, including the commonly used models and calculating tools for offshore structures can be found in [29]. For TLP FOWTs, the mooring system is especially vital for ensuring the safety of the whole structure since self-stabilisation cannot be achieved without tendons. In other words, the loss of tendons may result in the loss of the whole system. The previous research and design experiences reveal that the mooring failure condition has been one of the most determining load cases for the design of the floating platform and mooring system. The design guidelines

and standards for FOWT, such as [30-33] have addressed the importance of analysing mooring failure impact on the system. Due to the poor accessibility of floating wind farms, the system may be in its damaged state for hours or days until the broken mooring/tendon is fixed, and this is especially dangerous for TLP whose stability highly relies on its mooring system. Therefore, it must be ensured that the long-term stability of the platform under mooring failure conditions is well sustained to prevent the progressive failure of the mooring system, the loss of power and even the destruction of the whole facility [34].

Although no accidents have been reported yet in the FOWT industry, as the number of commercial-scale installations is small, mooring line failure cannot be ruled out from the research and design stages. Cases have been reported in the oil and gas industry, although their technology is much more mature than that of FOWTs. In the oil and gas (O&G) industry, damage to the floating drilling units and production platforms in the Gulf of Mexico (GOM) from hurricanes Katrina and Rita was reported in [35]; nineteen mobile offshore drilling units lost their moorings and became adrift during the storm, and the drifting platforms damaged 100 pipelines. The other representative case occurred on 29 May 2014, when six tendons of Chevron's major drilling project in the US GOM failed and led to subsequent damage to three additional tendons in subsequent days. The accident directly resulted in a construction delay of four years [36]. Research has been widely undertaken for understanding the risk of mooring failure on the O&G floating platform and to propose operating and emergency procedures, maintenance requirements, and design practices against the accident [35]. The studies identified that the reduction of mooring restoring forces due to mooring failure can be varied for different configurations of platform and mooring systems. The change in mooring restoring properties subsequently leads to the variation of tension force, the change in the mean position and the motion of the platform [37, 38]. In some cases, the super-harmonic resonance of the platform can be excited due to changes in the natural period after mooring breakage [39, 40]. For TLP FOWT, the effect of tendon failure can be more serious since the

wind turbine is a typical high-rise structure that may lead to significant overturning moment. It was found that for an inclined-tensioned TLP FOWT, when two or more tendons fail, there is a risk of collapsing [41-43]. The research pointed out that the mooring system should be carefully optimized to sustain the ability to withstand environmental loads under the failure condition.

Due to the combined effects of wind, waves and the coupling between different substructures, the responses of FOWTs after tendon failure can be more complicated. Few studies have been carried out to investigate the effect of mooring failure on the global performance of the FOWTs. Bae et al. investigated the performance change of a semi-submersible FOWT after one mooring line failed [44]. The results showed that the platform was subject to a large drift along with the wind and wave incident direction. The mooring failure effect on the transient response of a spar-type FOWT was studied by Li et al. Similar to the semi-submersible platform, a significant drift of the platform was observed, which could cause a risk of collision with the neighbouring turbine in the wind farm [45]. Wu et al. studied the transient response of the WindStar TLP FOWT with one tendon failure [46]. The results showed that the effect of tendon failure on TLP is different from that on the spar and semi-submersible FOWTs. The most significant change was observed in the increase in tendon forces rather than the platform offset. It was also found that the transient responses of the platform and the turbine under the operational conditions are higher than that under the extreme condition corresponding to the 50-years return period. The significant change in tension force led by the failure of one tendon has also been reported in [47]. Ren et al. studied the performance of a newly designed TLP FOWT under the mooring failure conditions using numerical approach [48]. The study demonstrated the feasibility of TLP FOWT being deployed in an intermediate water depth. Significant changes in the platform's responses and forces in the unbroken tendons were observed and indicate the importance of the analysis of tendon failure effects for TLP FOWT.

The above-mentioned studies illustrated that the mooring/tendon failure can affect the performance of a floating wind turbine in terms of the drift of the platform, the transient increase of structural response and the rise of tension force in the remaining mooring system. However, at present, all the published work about mooring failure analysis of FOWT were based on numerical modelling. For such a complicated system under complex environmental conditions, only adopting the numerical-modelling based approach is insufficient. Investigation through the experiment is therefore desired to illustrate the tendon failure effects in a more solid way and to identify the extreme responses and the nonlinear phenomenon that is possible to be ignored by the numerical model [49].

The main scope of the present study is to investigate the performance of the TLP FOWT under combined wind and wave conditions, especially accounting for tendon failure, by experimental approach. A prototype 5-MW wind turbine supported by a multi-column tension leg platform at an intermediate water depth of 60 m was scaled to a ratio of 1:50 based on the Froude law and tested in a wave basin. The outline of this paper is given as follows. In Section 2, the dimensions of the prototype and the scaled model, the settings of the experiment, and the environmental conditions are described in detail. The platform motions and tendon forces obtained from the experiments are presented and discussed in time and frequency domains in Section 3. Also, the effect of tendon failure on the performance of the FOWT are illustrated. Conclusions derived from this study are summarised in Section 4.

2. Experiment description

2.1. Prototype of FOWT

A novel tension leg platform was designed based on the conventional tri-floater platform to support the NREL offshore 5-MW baseline wind turbine. Detailed design considerations may be found in [48]. As shown in Fig. 1, the platform consists of (1) three cylindrical columns,

(2) three heave plates attached at the bottom of the columns, (3) a centre column placed at the middle of the platform linked with main columns through several beams and braces. The turbine is connected to the platform via the centre column, whose diameter is the same as the tower base. One column is positioned upwards to the incident waves, and the rest are in the leeward direction, while the wind and waves are assumed to be aligned along the positive X-direction.

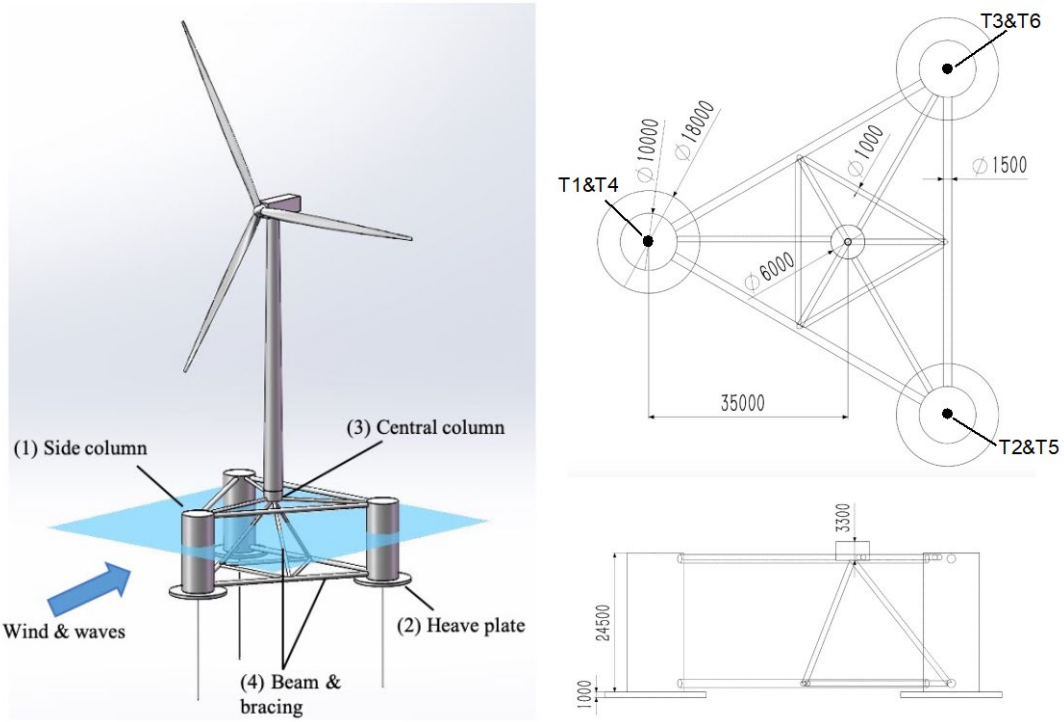

Fig. 1. 3D sketch of the FOWT (left), top and side views of the platform (right) (dimensions are in mm).

Synthetic fibre rope was selected for constructing the tendon because of its high elasticity and breaking load. The ropes are attached at the bottom centre of the heave plate, with one pair of lines on each column. Ropes are numbered in a clockwise direction, as illustrated in Fig. 1.

2.2 Model scaling

The test model used for the experiment was scaled down following the Froude law. The scaling factor was determined to be 1:50 considering the capability of the tank and the wavemaker. The geometrical similarity between a prototype and a physical model can be achieved by

$$L_p/L_m = \lambda \tag{4}$$

where, λ is the scaling ratio, L_p and L_m are any two corresponding homologous dimensions of the prototype and the physical model. The subscripts p and m denote the parameters for the prototype and the physical model respectively. According to the Froude Law, the kinematic and dynamic properties should satisfy the relationship:

$$\frac{{V_p}^2}{gL_p} = \frac{{V_m}^2}{gL_m} \tag{5}$$

where ${V_p}^2$ and V_m are velocity and g is the gravitational acceleration. It is to be noted that, the water density in the test basin is different from that of the seawater, thus a ratio between the water densities (γ = 1:1.025) should be taken into consideration when designing the physical model. Table 1 shows the scaling ratios for different parameters determined to satisfy the above-introduced similarities.

Table 1. Scaling ratios for different dimensions following the Froude Law.

Dimensions	Scaling ratios	Conversion
Length	λ	1:50
Angle	λ^0	1:1
Volume	λ^3	1:125000
Time/period	$\lambda^{0.5}$	1: $\sqrt{50}$
Velocity	$\lambda^{0.5}$	1: $\sqrt{50}$
Acceleration	λ^0	1:1
Force	$\gamma\lambda^3$	1:128125
Mass	$\gamma\lambda^3$	1:128125
Moment of inertia	$\gamma\lambda^5$	1:320321500

Gravity	λ^0	1:320321500

The above scaling ratios have been applied for this study. The dimensions of the test model and the full-scale model are summarised in Table 2. The measured dimensions of the tested model are compared with the aimed value calculated according to the scaling ratio and the errors are listed in the table. The errors for the size of the component, such as the height and radius of the column and heave plate, the length of the tower, etc., are less than 6%. The total mass of the fabricated platform is 14.9 kg, which is 2.6% higher than the aimed value. The tower mass of the scaled model is 30% higher than the aimed value and this part of the weight is compensated by reducing the mass of the rotor disk. Several clumped masses are distributed inside the platform to match the moment of inertia of the whole structure. Thus, the overall similarity of mass distribution between the scaled model and the prototype was retained.

Table 2. Dimensions of the test model and the full-scale model.

Parameter	Prototype	Aimed value	Measured value	Error
Platform mass	1.86E6 kg	14.51 kg	14.90 kg	2.6%
Side column height	24.5 m	0.49 m	0.489 m	-0.2%
Side column radius	5 m	0.10 m	0.10 m	0.0%
Heave plate radius	9 m	0.18 m	0.18 m	0.0%
Heave plate height	1 m	0.02 m	0.021 m	5.0%
Draft	16.5 m	0.33 m	0.35 m	6.0%
Platform vertical centre of mass below SWL	8.65 m	0.173 m	0.165 m	-4.6%
I_{xx}/I_{yy}	1.21E9 kgm^2	3.77 kgm^2	3.34 kgm^2	-11.5%
I_{zz}	2.209E9 kgm^2	6.90 kgm^2	5.84 kgm^2	-15.3%
Tower length	77.6 m	1.552 m	1.550 m	-0.1%
Tower mass	249718 kg	1.949 kg	2.5387 kg	30%

RNA (drag disk) mass	350000 kg	2.732 kg	2.5033 kg	-8.4%

2.3. Facilities

Tank testing of the FOWT was conducted at the State Key Laboratory of Coastal and Offshore Engineering at Dalian University of Technology. The tank has a length of 60 m and a width of 4 m. The water depth is 1.2 m in this experiment. The test model was installed in the middle of the tank, as shown in Fig. 2, where the waves have fully developed, and the effect of reflection was relatively small. Seven wave probes were installed to measure the properties of the incident waves at different positions. Probe WP3 was positioned at the centre of the tank and only used during wave calibration. The wave probes were of capacitance type and their installation and arrangement are shown in Fig. 3. A 750 × 750 mm axial fan was installed 3 metres in front of the model to generate a wind field.

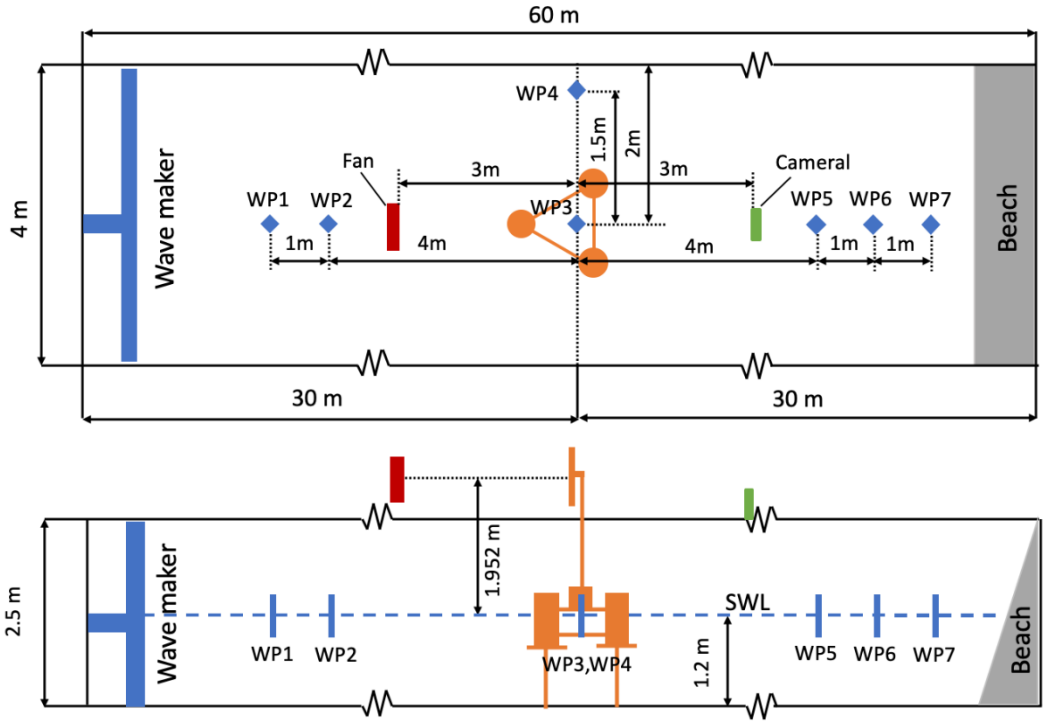

Fig. 2. Illustration of the tank and facility arrangement (Plan view and side view)

Fig. 3. Photos of wave probes installed in the wave tank

As shown in Fig. 4, the main body of the platform (1) was made of carbon fibre, which is a material that features high strength and stiffness. Tower (2) consists of a steel tube and a flange connecting to the central column of the platform. Since the present study mainly focuses on the hydrodynamic performance of the platform, the RNA was simplified as a drag disk (3) fabricated with wood to model the rotor thrust. A square steel plate was welded on the top of the tower and the drag disk was installed on the plate as shown in Fig. 5. An accelerometer (4) was installed on the top of the tower to measure the tower top acceleration.

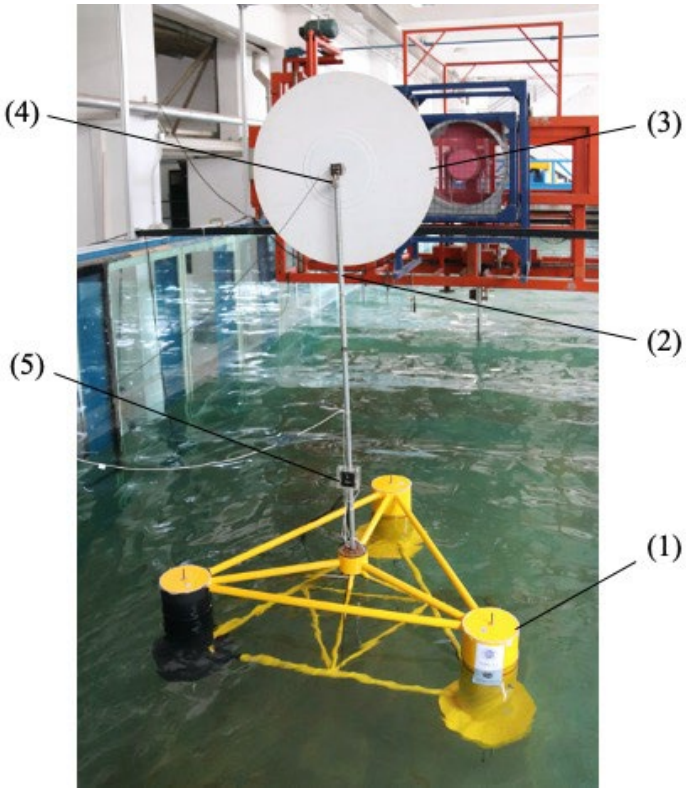

Fig. 4. Experiment model of the TLP FOWT installed in the wave tank

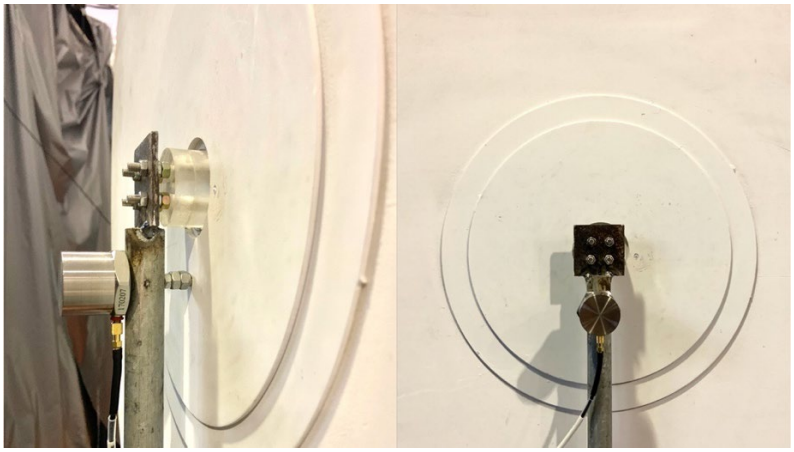

Fig. 5. Connection between drag disk and tower

The motion of the structure was captured by an NDI Optotrack Certus optical tracking system. A marker (5) was attached to the tower at a height of 200 mm above the tower base. The 6-DOF motions of the marker were measured by an infrared camera and transformed to the motion of the platform, assuming that the tower and the connection between the tower and the platform were rigid. It should be noted that the wall thickness of the columns and

the beams were not scaled by the ratio of 1:50 due to fabrication limitation. The mass distribution was adjusted accordingly by the clumped weight installed inside the column considering the mismatch of the wall thickness. The tower mass of the scale model was 30% higher than the aimed value, while this part of the weight was compensated by reducing the mass of the rotor disk. The similarity between the scale model and the prototype in the overall mass distribution of the disk and the tower was retained.

The left diagram of Fig. 6 illustrates the components used to construct the mooring system. Six steel wires were connected with springs to achieve the equivalent axial stiffness of the tendon. The tendon forces were measured by water-proof load cells installed just above the anchor position. The dimensions of the mooring system in full and model scales are listed in Table 3.

Table 3. Parameters of mooring system of the model.

Parameter	Full-scale model	Test model
Diameter (mm)	245	2
Unstretched length (m)	43.295	0.82
Number	6	6
Axial stiffness (N)	2.75×10^8	2200
Mass density in air (kg/m)	430	0.15
Minimum breaking load (kN)	20307	N/A
Total pretension (kN)	28500	0.228

The failure scenario in the present study assumes that one of the six tendons is broken at an appointed time. To achieve transient tendon failure in the test, the model of the mooring system was specially designed. For each pair of tendons, one of the tendons was connected to the platform via an iron disc attached to a strong electromagnet (as shown in Fig. 7, left) installed on the bottom of the platform (the three tendons are indicated by T1, T2 and T3 as shown in Fig. 1), and, another one was connected to the platform directly with an eyebolt as shown in Fig. 8 (indicated by T4, T5 and T6). For T1, T2 and T3, steel wires were connected to

small disks made of Q235 steel (as shown in Fig. 8, left), which is a magnetic material and can be tightly attached to the electromagnet when it is powered up. The three electromagnets were controlled independently via adapters (as shown in Fig. 7, right). At the beginning of each test, all the electromagnets were switched on, so that all the tendons were connected to the platform at an intact state. Once a specified electromagnet is switched off, the tendon can immediately disconnect from the platform, which realise the scenario that the tendon broke at the fairlead position. The instruments used in the experiment are summarised in Table 4.

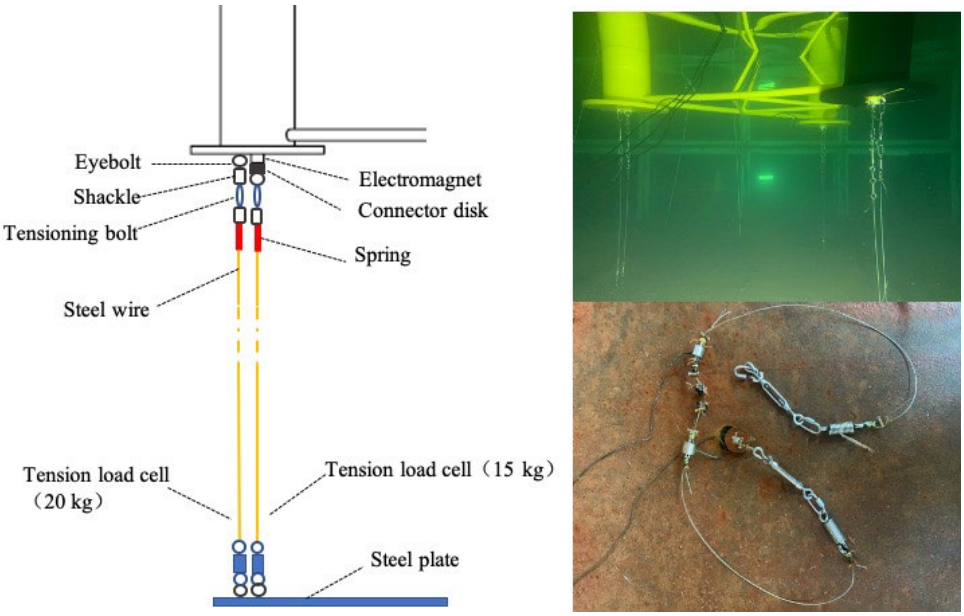

Fig. 6. Experiment model installed in the tank (left) and illustration of mooring system (middle and right).

Fig. 7. Electromagnet and power adapter

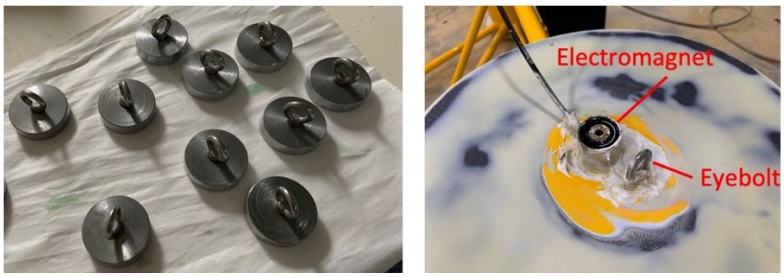

Fig. 8. Photos of steel disks used to attach to the electromagnet and installation of electromagnet and eyebolt

Table 4. Summary of measuring instruments.

Instrument	Measurement
Accelerometer	Tower top acceleration
NDI motion capture system	6-DOF motion
Wave gauge	Wave parameter
Tension load cell	Tendon tension

2.4. Load cases

The free-decay tests, regular wave tests (no wind) and wind-wave combined tests were carried out in the study. Free-decay tests were performed in calm water to verify the resonance properties and hydrodynamic coefficients for the FOWT.

A total of 18 regular wave conditions with different wave periods and heights were selected to obtain the platform's performance under the excitation of waves and to derive its response amplitude operators (RAOs). For each load case, the test was repeated twice and lasted for 3 min and 30 s for regular wave load cases. The detailed parameters of the regular wave load cases in model-scale and full-scale are shown in Table 5.

Table 5. Parameters for regular wave tests

Case name	Wave height H (m)		Wave period T (s)	
	Model	Full-scale	Model	Full-scale
RE1	0.04	2	1	7.071
RE2	0.04	2	1.41	9.97

RE3	0.06	3	1	7.071
RE4	0.06	3	1.25	8.839
RE5	0.06	3	1.5	10.607
RE6	0.08	4	1.25	8.839
RE7	0.08	4	1.77	12.5
RE8	0.1	5	1.25	8.839
RE9	0.1	5	1.5	10.607
RE10	0.12	6	1.25	8.839
RE11	0.12	6	1.5	10.607
RE12	0.12	6	1.77	12.5
RE13	0.14	7	1.25	8.839
RE14	0.14	7	1.5	10.607
RE15	0.16	8	1.5	10.607
RE16	0.16	8	1.75	12.374
RE17	0.18	9	1.75	12.374
RE18	0.2	10	1.75	12.374

To investigate the dynamic performance of the FOWT under the real stochastic ocean environment, and to address the problem of tendon failure on the FOWT, model tests were conducted in combined wind and wave conditions with intact and failed tendons. The wind and wave parameters were determined according to the China South Sea environment and the JONSWAP wave spectrum was utilised for modelling irregular waves. A total of four sets of environmental conditions were determined with the wave height ranging from 0.04 m to 0.2 m (corresponding to 2 m to 10 m in full-scale) and the wave period ranging from 1 s to 1.87 s (corresponding to 7.01 s to 13.2 s in full-scale). The wind and waves were assumed to be collinear.

As described in Section 2.3, the wind turbine was simplified to a drag disk to imitate the rotor thrust generated by the inflow wind. To produce the proper thrust force corresponding to each environmental condition, the wind speed generated by the fan was adjusted as follows:

1) Calculate the mean thrust force corresponding to each load case using the numerical simulation tool, FAST. The details can be found in [48].
2) Calculate the objective wind speed generated by the fan using the following equation:

$$v_m = \frac{\sqrt{\frac{2F_m}{\rho\pi}}}{r} \quad (1)$$

where v_m is the mean wind speed at hub-height in model scale, F_m is the mean rotor thrust corresponding to the full-scale wind speed v_p calculated by numerical simulation and transformed to model scale, ρ is the air density, which was taken as 1.29 kg/m^3 in this research, r is the diameter of the rotor disk, which was 0.375 m.

3) Calibrate and adjust the wind fan until the objective wind speed at the rotor position is achieved.

For each environmental condition, three tendon states were considered, those are intact tendon condition, T1 broken condition and T2 broken condition. Overall, twelve load cases were utilised in the present study with different environmental parameters and tendon states. Each load case was repeated three times. The detailed parameters for each case are described in Table 6. The specific tendon was modelled to be disconnected at 150 s out of the 330 s test by controlling the electromagnet as introduced in Section 2.3.

In the extreme sea state (LCs 4~6), the turbine remains still and the aerodynamic load acting on the turbine does not change much regardless of the tendon state. However, for the environmental conditions in that the wind speeds are within the operating range, the turbine is supposed to be rotating when the tendons are intact and shut down when the tendon breakage occurs. This can lead to a significant decrease in rotor thrust and should also be considered in the experiment. In the tendon failure tests, after the disconnection of the tendon, the wind speed was reduced to match the lower aerodynamic load for the parked wind turbine. As shown in Table 6, the wind speed reduces from 4.68 m/s to 1.87 m/s after

the tendon failure occurs under the environment with the rated wind speed and from 3.02 m/s to 2.00 m/s under the extreme environmental condition.

Table 6. Parameters for wind-wave combined test

No.	Full scale			Model scale			Tendon state
	H_S (m)	T_P (s)	V_{Hub} (m/s)	H_S (m)	T_P (s)	V_{Hub} (m/s)	
LC1							Intact
LC2	7.6	13.2	11.25	0.15	1.87	4.68 (1.87) *	T1 broken
LC3							T2 broken
LC4							Intact
LC5	10	10.2	41	0.2	1.44	2.26	T1 broken
LC6							T2 broken
LC7							Intact
LC8	5.4	7.5	25	0.11	1.06	3.02 (2.00) *	T1 broken
LC9							T2 broken
LC10							Intact
LC11	4.928	10	11.25	0.10	1.41	4.68 (1.87) *	T1 broken
LC12							T2 broken

Note: * The number in the bracket indicates the reduced wind speed after tendon failure.

3. Results and discussion

The results obtained from the experiment are illustrated and discussed in this section. All the data are presented in full-scale.

3.1. Free-decay tests

The results of free-decay tests are shown in Figs. 9-11. The natural periods of platform surge, heave and pitch are calculated to be 20.291 s, 1.41 s and 3.44 s respectively, which is in-line with the typical range recommended by DNV-ST-0119 (15~60 s, 1~2 s and 2~5 s) [30].

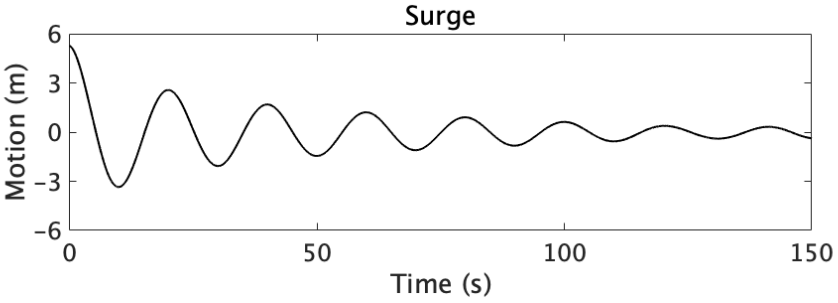

Fig. 9. Free-decay curve of platform surge.

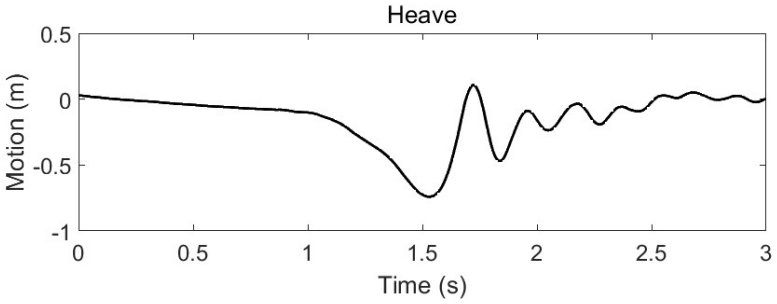

Fig. 10. Free-decay curve of platform heave.

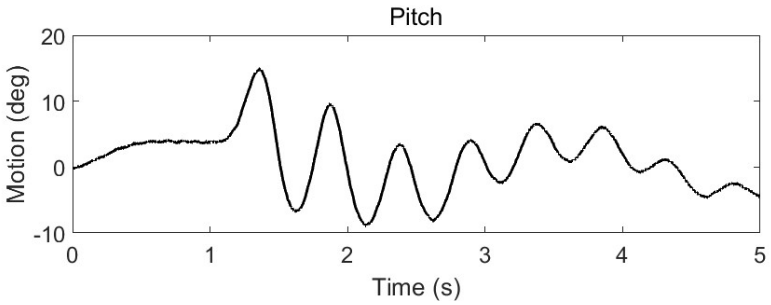

Fig. 11. Free-decay curve of platform pitch.

3.2. Regular wave tests

A total of 18 regular wave load cases were employed in this experiment to evaluate the response of the TLP FOWT. Taking the load case RE1 as an example (H = 2 m, T = 7.071 s), the wave elevations, platform motions in surge, heave and pitch, and the tension forces in the tendons were measured and the results are shown in Fig. 12. It can be seen from the plots that the data obtained from the two repeated tests are consistent. The platform motions and the tension forces fluctuate regularly along with the incident waves.

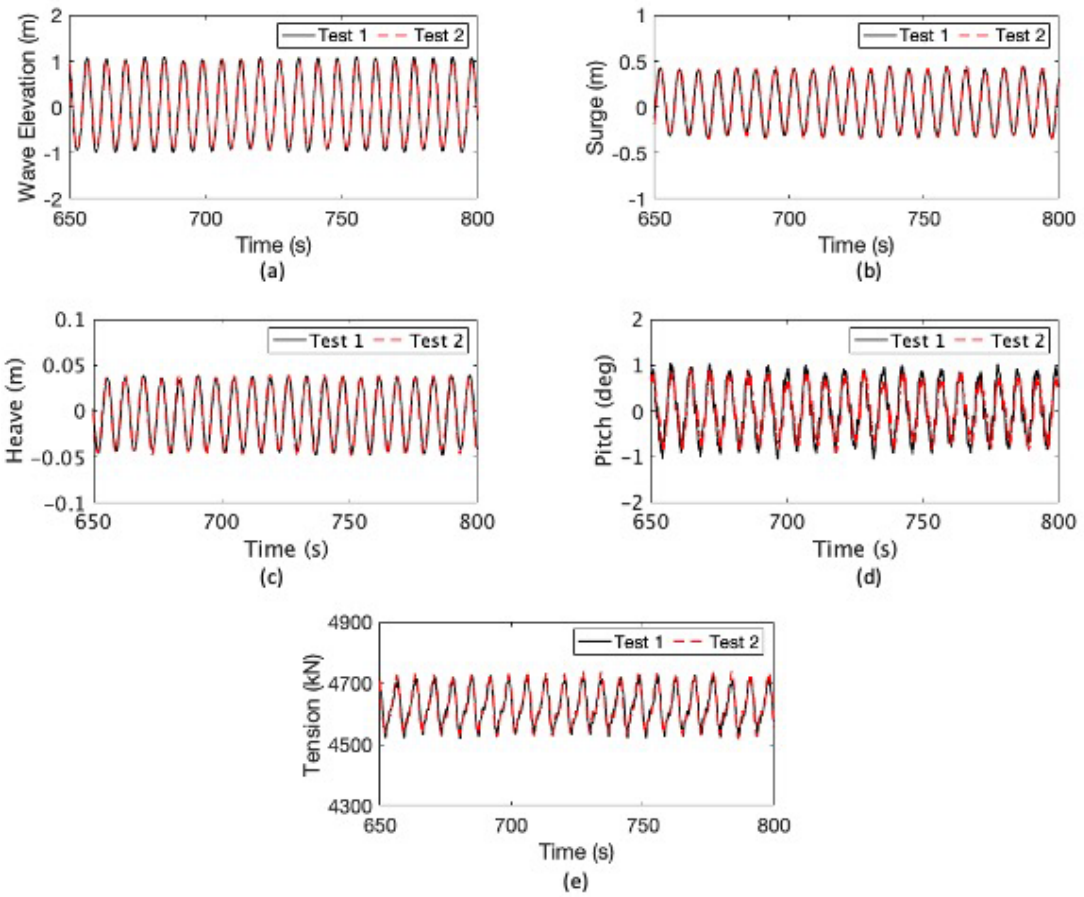

Fig. 12. Results of RE1 test: (a) Wave elevations; (b) Platform surge responses; (c) Platform heave responses; (d) Platform pitch responses and (e) Tension forces in tendon T6

The RAOs of platform's surge, heave and pitch for regular wave tests are shown in Fig. 13. Higher values of response are observed for surge, while the heave and pitch motions are found to be smaller due to taut moored tendons. The largest nondimensional surge response reaches 1.5 m/m, corresponding to the longest wave period (12.5 s). The response in heave is mainly due to the coupling between platform surge and heave, i.e. setdown effect [48]. The pitch RAO remains below 0.3 degree/s, indicating the stability of the platform in the rotational mode.

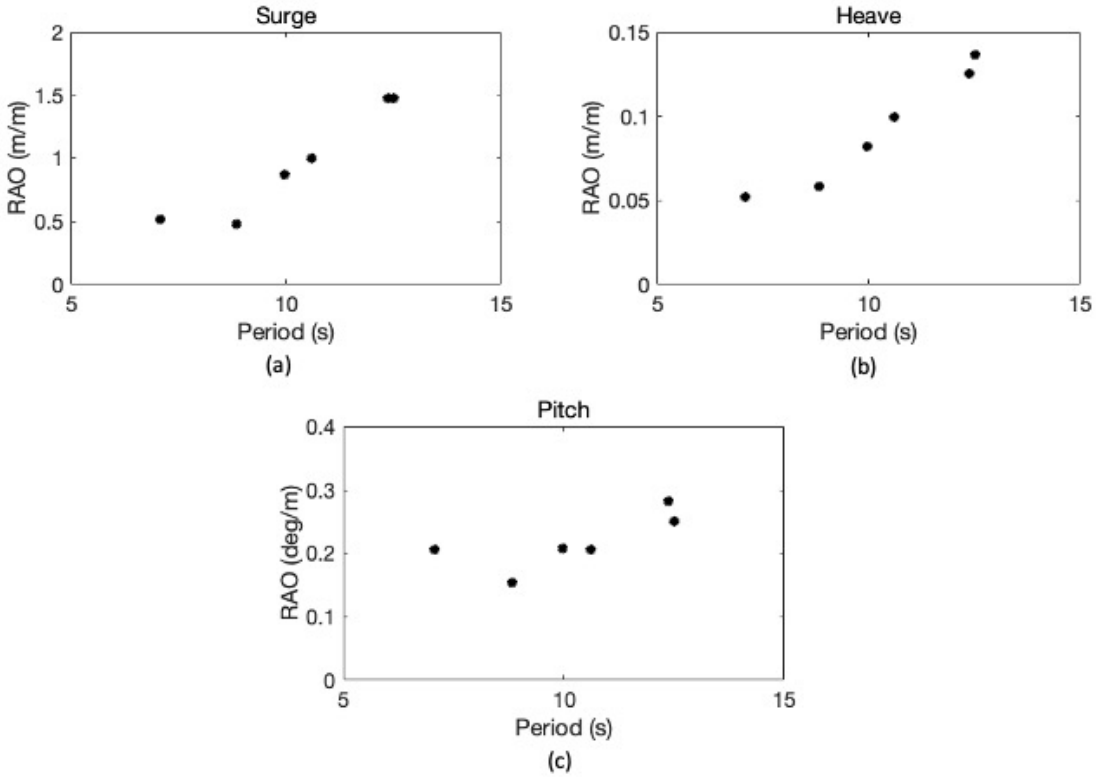

Fig. 13. RAOs of platform surge (a), heave (b) and pitch (c)

3.3. Wind-wave combined load cases

The platform motions and the tension forces in the tendons for the 12 wind-wave combined load cases are presented in this section. The wave elevations measured by the wave probe WP3 in time series and their spectrum derived by MATLAB FFT algorithm are shown in Fig. 14.

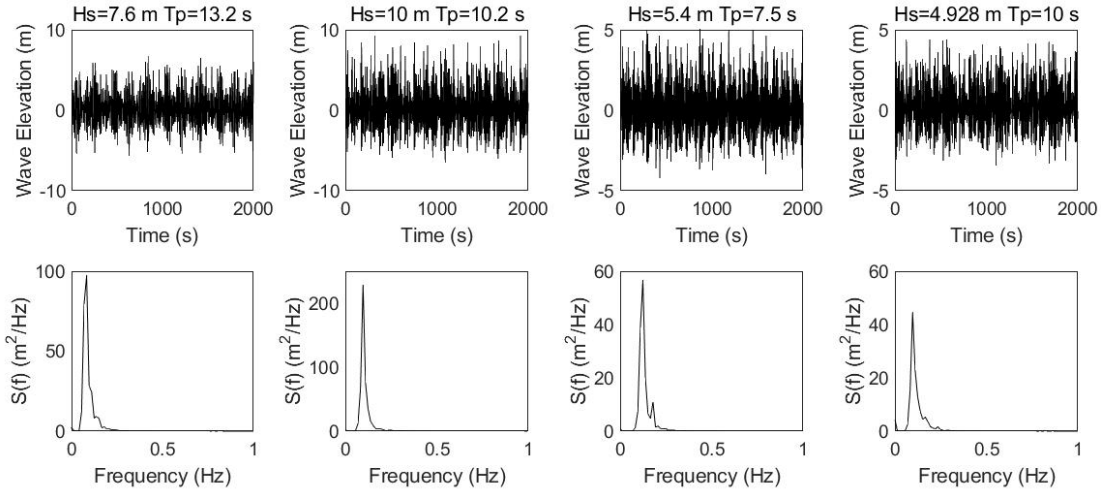

Fig. 14. Time-series wave elevation and spectrum.

3.3.1 Platform motion analysis

The time-series responses and power density spectra (PSD) of the platform surge for LCs 1-12 are illustrated in Fig. 15. The tested data obtained with the intact tendons (LC1, LC4, LC7 and LC10) are compared with those with broken tendons and the statistics derived by the time-series results are presented in Fig.16. The most significant surge responses are observed in LC1-3, corresponding to the operating environmental condition with a significant wave height of 7.6 m/s, the peak period of 13.2 s and the mean wind speed of 11.25 s (full scale). The peak energy of the spectra is seen at the wave frequencies of 0.089 Hz, 0.098 Hz, 0.133 Hz and 0.1 Hz, respectively, showing that the surge responses of TLP FOWT are dominated by the excitation of waves. The highest energy density at wave frequency is seen in Fig. 15 (b) (for LC1) when the turbine is operated at rated wind speed, and the wave period is the longest among all four cases. A smaller peak can be found for LCs 4-12 in Fig.15 (d) (f) and (h) at the platform surge natural frequency (i.e., at 0.05 Hz). The corresponding energy contents are at the same level for the three cases, being about 5 m2/Hz. Since the power density for LC1 at the wave frequency is much higher than that at the platform surge natural frequency, and the two frequencies are close to each other, the secondary peak seen for LCs 1-3 at the platform's surge natural frequency is not observed here.

For most of the cases, the failure of one tendon did not lead to an obvious change in the platform's surge response in both time- and frequency-domain. The mean surge position has a slight downward drift after the time point of failure for LC7 to LC12. The mean value reduced from 0.16 m for LC7 (intact tendon) to -0.15 m for LC8 (T1 broken) and -0.32 for LC9 (T2 broken). The most significant change in surge with failed tendon is observed for LC11 (i.e., T1 failed) and LC12 (i.e., T2 failed), for which the mean surge value decreased by 1.36 m and 1.67 m respectively. However, the main reason for the change in mean surge motion may not be related to the tendon failure, but the reduction of aerodynamic load acting on the rotor (drag disk). By calculations based on FAST, the rotor thrust decreased by 84% when the rotor is shutdown at the rated wind speed (11.25 m/s), and by 56% at the cut-out wind speed (25 m/s). Therefore, the reduction of motion was most significant when the rated wind speed was applied. For load cases LC4 to LC6, the state of the turbine did not change, and the aerodynamic load remained

at the same level, and the change of surge motion was not observed. Meanwhile, for load cases LC1 to LC3, although the aerodynamic load also had a remarkable decrease, as the wave condition was much harsher than that used for LC10 to LC12, the effect of rotor thrust was relatively insignificant and not evidently seen.

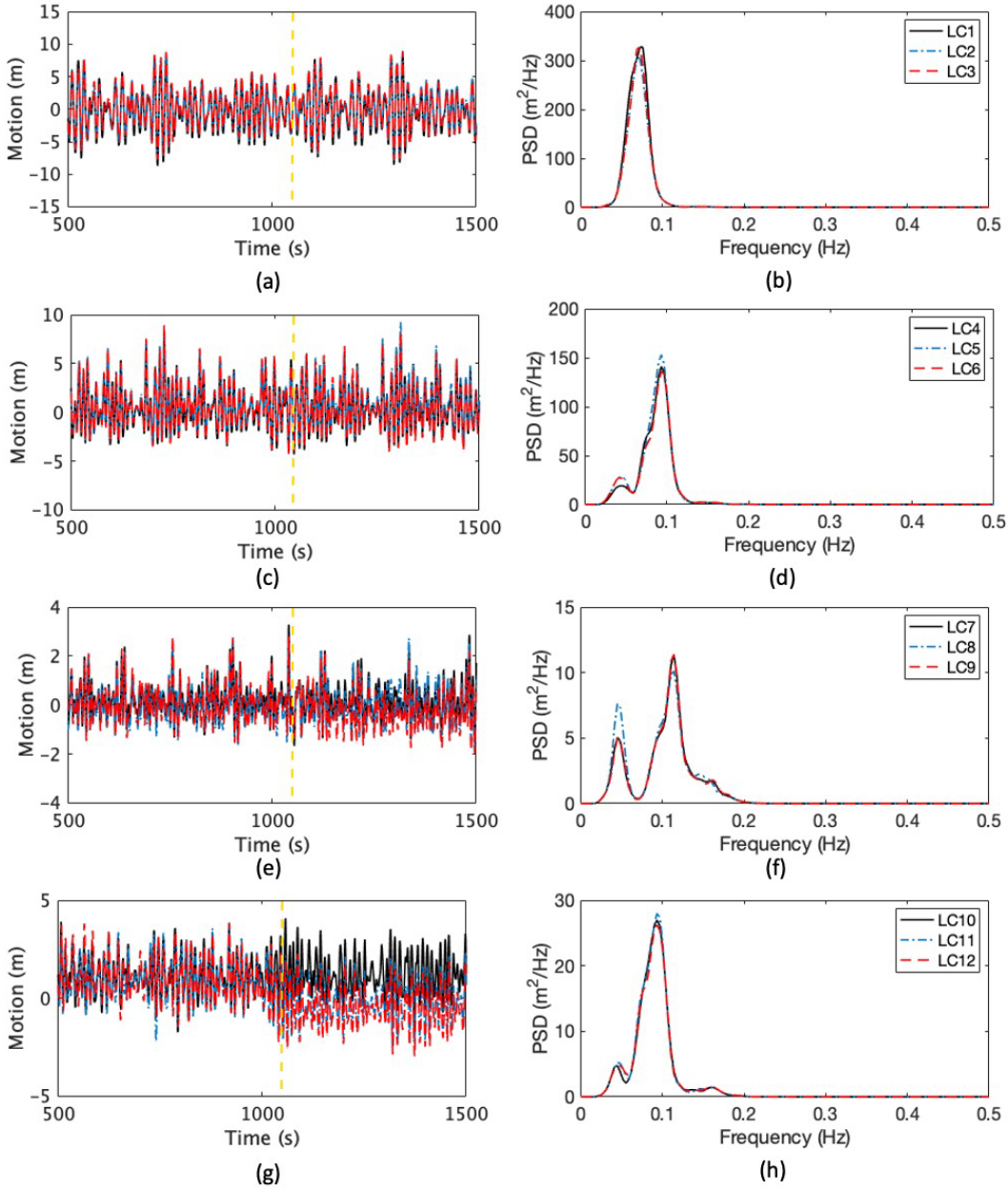

Fig. 15. Platform surge motions and PSDs for LC1-3 (a-b), LC4-6 (c-d), LC7-9 (e-f) and LC10-12 (g-h).

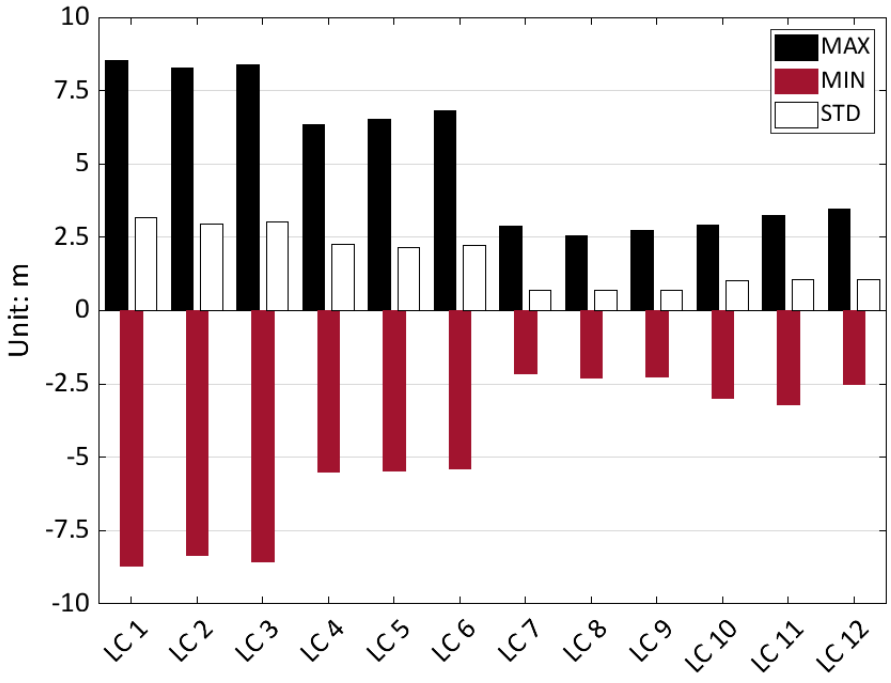

Fig. 16. Statistics of platform surge motion based on experimental results.

The platform heave motion obtained by the experiment and the corresponding PSD diagrams are illustrated in Fig. 17. The plots show a much smaller response in heave than that in surge due to the action of taut mooring system. The heave motion was within the range of -0.5 m to 0.7 m in all cases. The maximum heave amplitude observed in Fig. 17 (c), was related to the case tested with the operational environmental condition. An increase in heave motion is obvious in all the cases after one tendon has failed. However, as the loss of tension force in one tendon can be compensated by the increase of tension in other tendons, the maximum increase of mean heave is only 0.24 m. The PSD curves illustrate that the amplitudes and the peak frequencies are similar between each group of cases, indicating the slight effect of tendon failure on the platform's heave response.

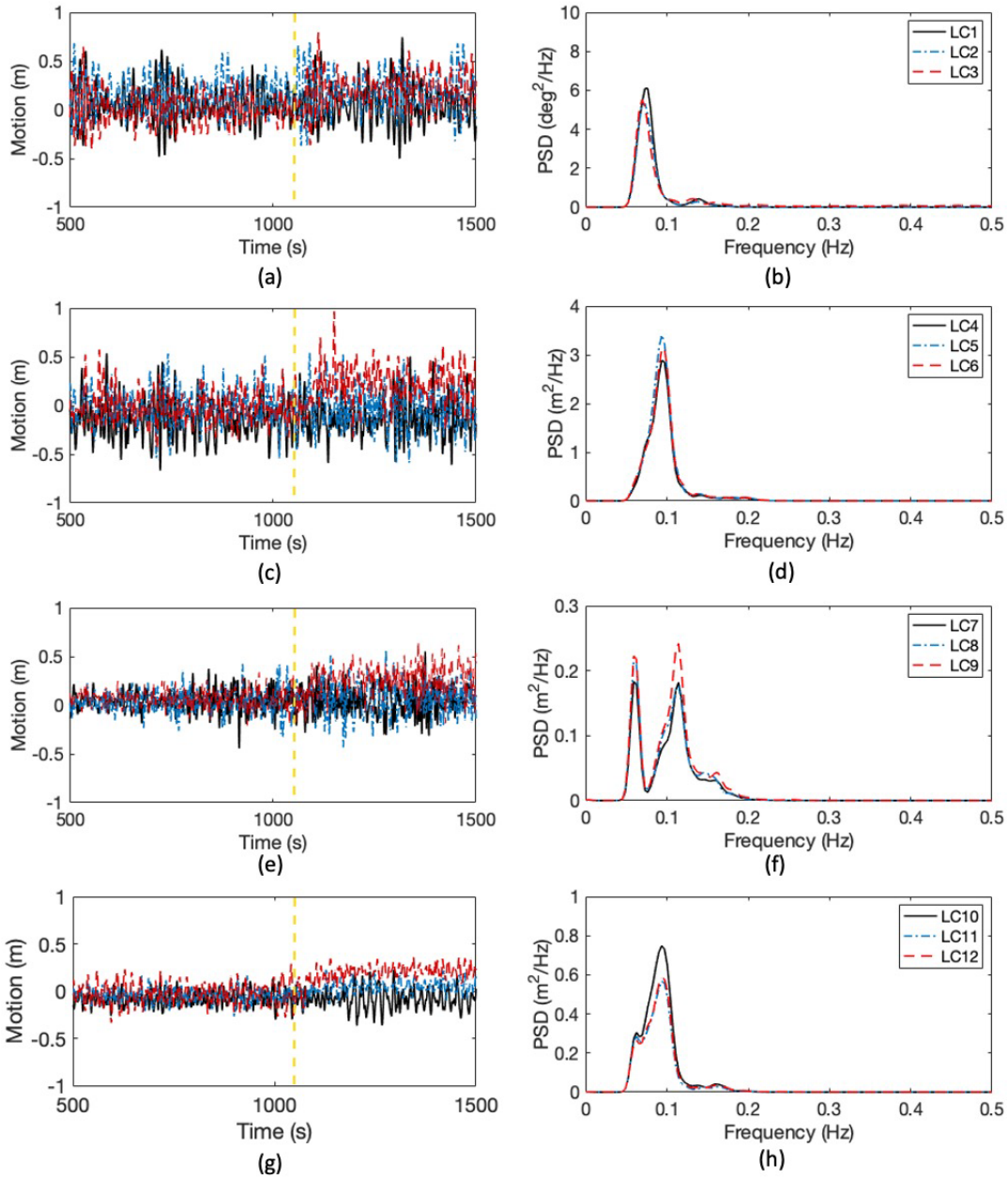

Fig. 17. Platform heave motions and PSDs for LC1-3 (a-b), LC4-6 (c-d), LC7-9 (e-f) and LC10-12 (g-h).

Fig.18 presents the platform's pitch responses for the 12 load cases as in Fig 16. The pitch motion remained between -1 and 2 degrees even under the tendon failure conditions, indicating a good stability of TLP in rotational mode. A decrease in average pitch occurred after the tendon break for cases LC1-LC3 and LC10-LC12, where the failure happened with the turbine rotating at the rated wind speed (11.25 m/s) and the rotor thrust is highest. After the tendon failed, the turbine was shut down in a state of emergency and the rotor thrust decreased significantly. Therefore, the change of pitch motion was not significant for the cases where the

turbine was parked under the extreme environmental condition or the wind speed was at its cut-out speed, relating to a lower rotor thrust during operation.

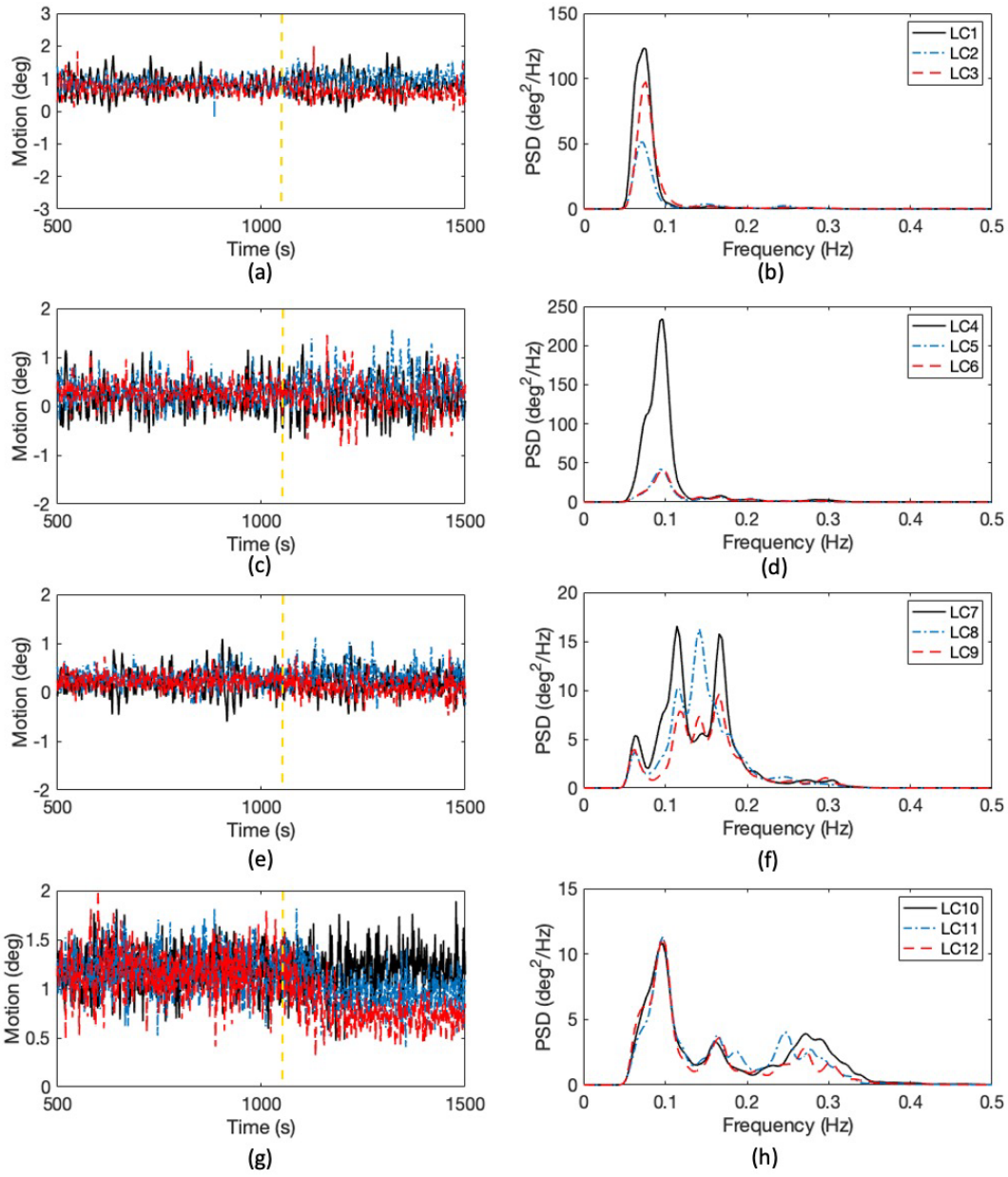

Fig. 18. Platform pitch motions and PSDs for LC1-3 (a-b), LC4-6 (c-d), LC7-9 (e-f) and LC10-12 (g-h).

The spectra of the platform pitch responses demonstrate that the energy density decrease at the wave period after one of the tendons failed for LC1-9. For LC 7-9. For LC 1-6, as the wave-induced motion is relatively drastic, the peaks at the platform's pitch natural frequency are rarely

seen. In Fig.16 (f) and (h), it can be observed that the failure of the tendon can lead to a shift of natural frequency. This is because the dynamic characteristics of TLP are closely related to the tendon properties. Thus, the change in tendon number, i.e. change in total tendon stiffness, alters the platform pitch damping stiffness. Once the tendon failed, the natural frequency in pitch gets close to the typical wave period and this may lead to a resonance (which is not seen in this study).

3.4. Tension force analysis

The tension forces are presented in this section. Fig. 19 illustrates the tension forces in tendons T1 and T2 between 500 s to 2000 s for LC1, LC4, LC7 and LC10 (intact tendon cases). For LC1 and LC4, where the wave heights are relatively large, the amplitude of tension in tendon T1 is comparable to that in T2. Nevertheless, higher amplitudes are observed in T1 than that in the load cases with lower wave height (LC7 and LC10).

Tendon slack was not observed in all cases, indicating that the design of the FOWT satisfies the corresponding requirements in terms of position mooring. In addition, the tension forces in all tendons do not exceed the minimum breaking loading, i.e., the safety of the mooring system is sustained under the above utilised sea states when the tendons are intact.

The power spectral densities (PSDs) for the tendon forces in T1 and T2 corresponding to the intact tendon load cases (LC 1, LC4, LC7 and LC10) are shown in Figs. 20 and 21. The results show that the PSDs for the four cases peak at their wave frequencies, that are, 0.076 Hz, 0.098 Hz 0.133 Hz and 0.076 Hz, respectively. The energy density of tension forces in T1 is the highest for LC4, corresponding to the most extreme environmental condition (highest wave height and mean wind speed). The similar shapes of the PSD curve for T2 can be observed in Fig. 21, while the amplitudes are lower than that for T1.

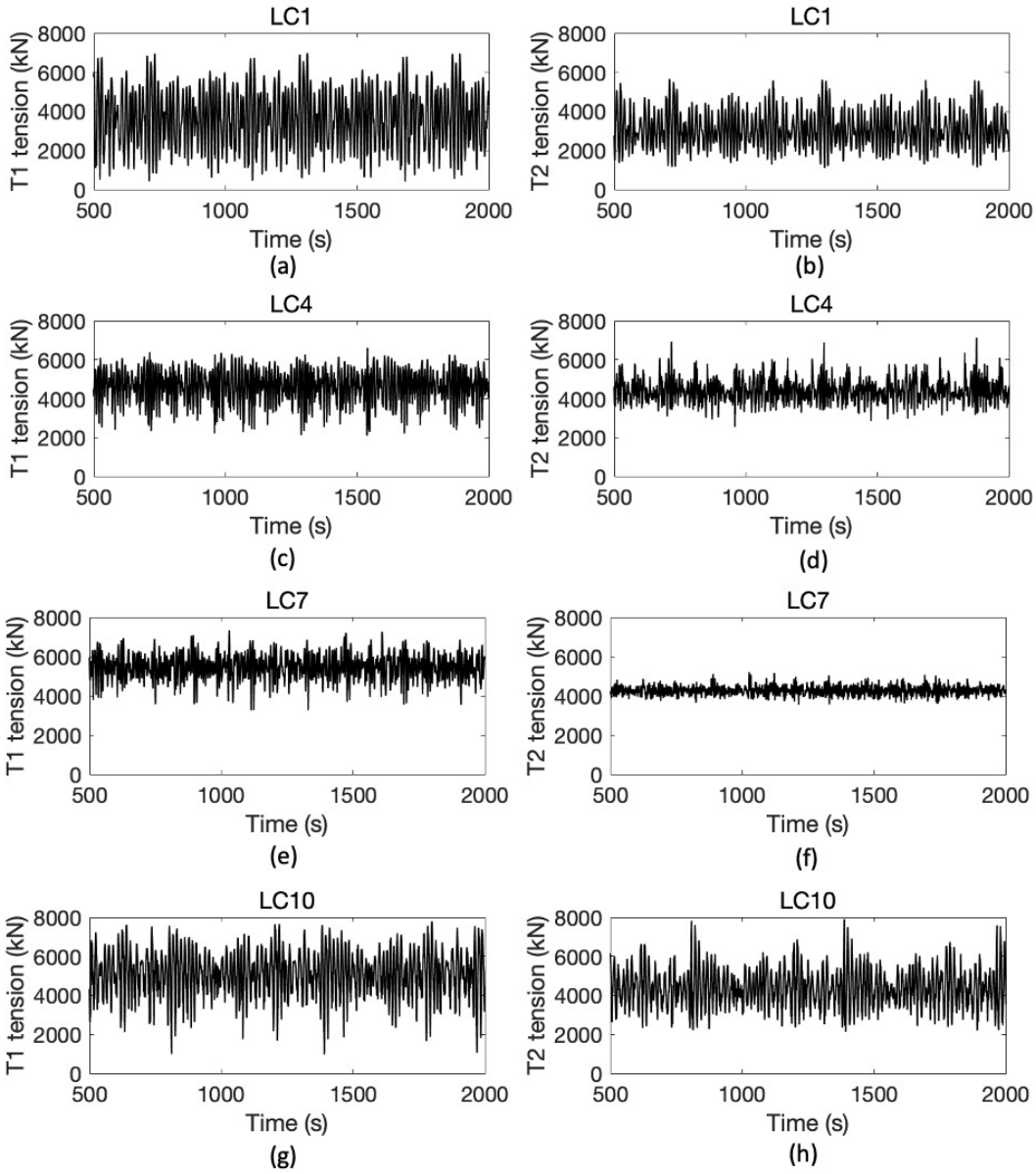

Fig. 19. Tension forces in T1 and T2 under intact conditions (LC 1, 4, 7 and 10).

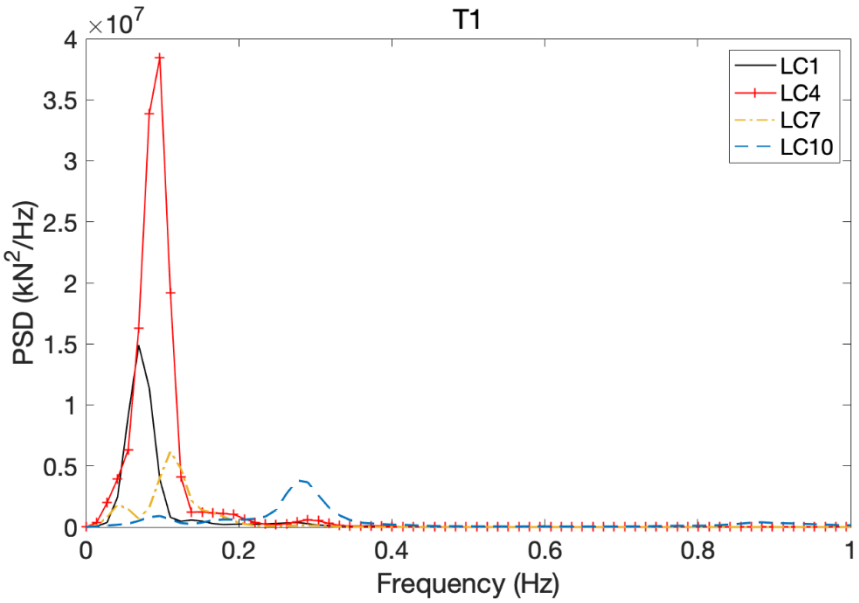

Fig. 20. PSD of tension forces in T1 for LC 1, LC4, LC7 and LC10.

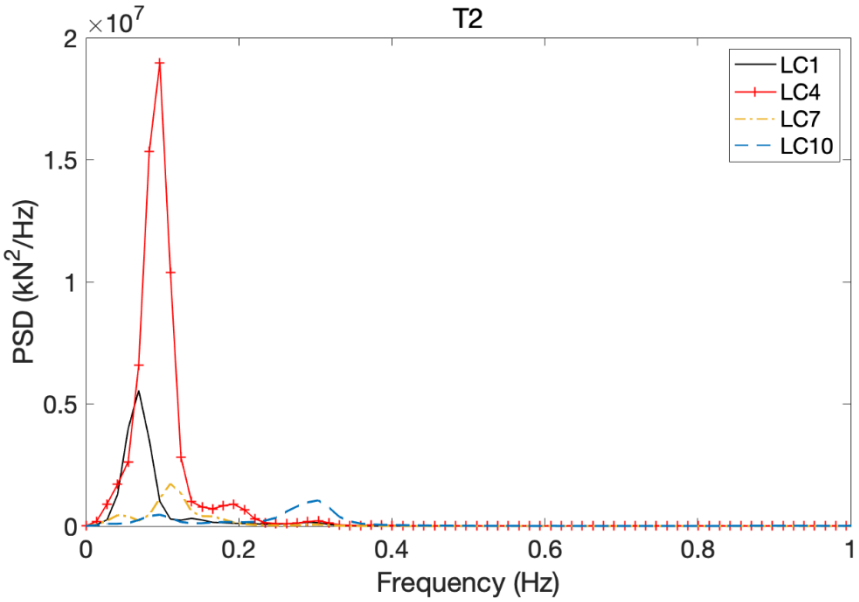

Fig. 21. PSD of tendon forces in T2 for LC1, LC4, LC7 and LC10.

For the tendon failure cases, the results show that the most remarkable effect of tendon failure is the change in tension forces in the remaining tendons. As a pair of tendons are attached at one column, when one of the tendons is broken, the adjacent one suffers from a significant increase of tension force, as depicted in Figs. 22 and 23. For LC2, LC5, LC8 and LC11, tendon T1 was broken at 1050 s, and special attention was paid to the adjacent tendon, i.e. T4 (see Fig. 22), while for LC3, LC6, LC9 and LC12, the tension forces in T5 are of interest as T2 is

broken (see Fig. 23). It can be observed that the tension forces in the adjacent tendon raise suddenly at the moment of tendon breakage. The average tension force and the amplitude of variation remain at a higher level after the breakage.

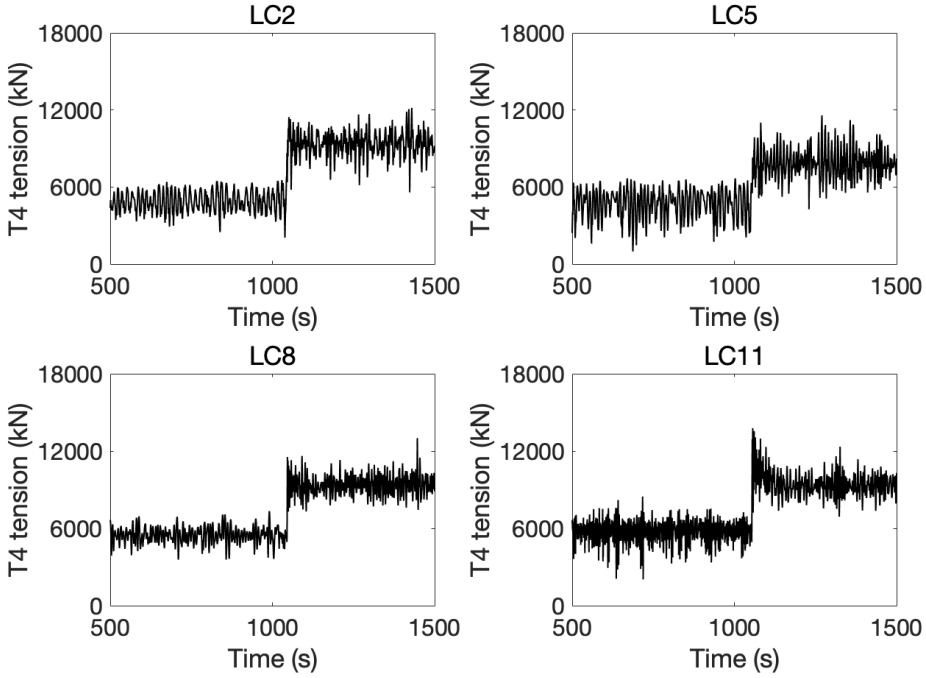

Fig. 22. Changes on tension forces in T4 for LC 2, LC 5, LC 8 and LC11 when T1 was broken.

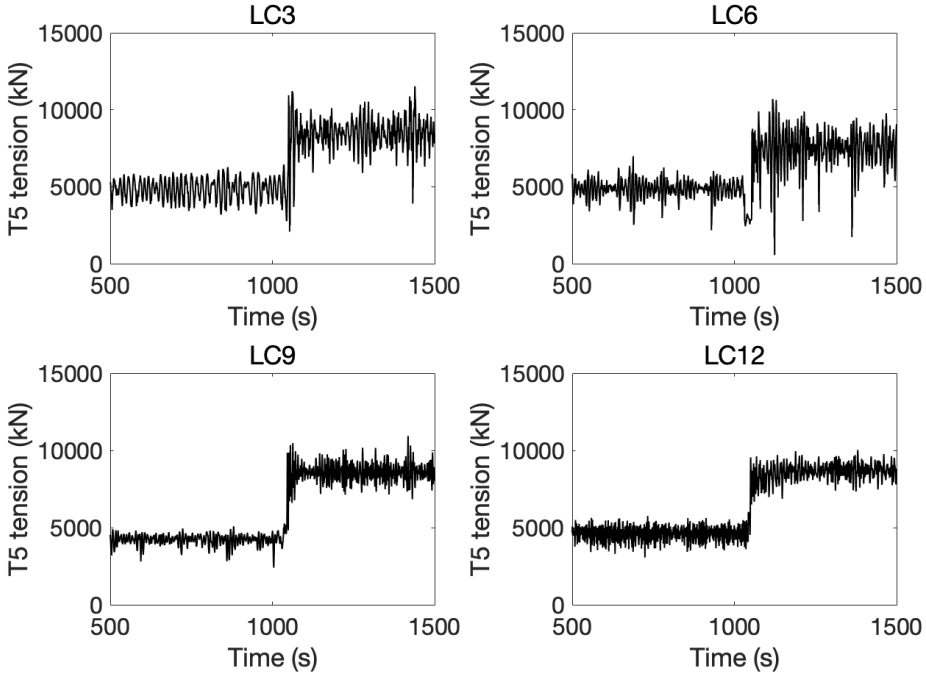

Fig. 23. Changes on tension forces in T4 for LC 3, LC 6, LC 9 and LC12 when T2 was broken.

To further investigate the impact of tendon failure on the force in the remaining intact tendons, the maximum, minimum, mean and standard deviation values of to the results before and after tendon failure occurs were calculated based on the experimental results. The data were normalised by dividing the corresponding value for the failure condition by that for the intact tendon condition to depict the ratio of change resulting from tendon failure. The higher the value is the more significant the tendon failure acting on the tendons. The normalised data are presented in Table 9. The largest increase in maximum tension is observed in LC5, in which the normalised effect under the tendon failure condition is 2.289 for the simulation and the experiment, i.e. the maximum tension force is 2.289 times in the accidental condition of that in the intact condition. For all the load cases, the ratio of maximum tension before and after tendon fails, and the STD values obtained by the simulations are higher than that derived from the measured data. The mean tension forces in T4 increase by over 68% after the failure of tendon T1 and more than 91% for T5 after T2 fails.

Table 9. Normalised statistics of tension forces.

Tendon No.	Load case	Max	Mean	STD
T4	LC 2	1.862	1.957	1.291
	LC 5	2.289	1.997	2.623
	LC 8	2.031	1.802	2.653
	LC 11	1.780	1.682	1.465
T5	LC 3	1.918	1.777	1.549
	LC 6	1.903	1.747	1.380
	LC 9	2.226	2.060	3.361
	LC 12	2.119	2.256	1.777

Therefore, it is vital to examine whether progressive damage would be caused to the high-risk tendon. The dynamic safety factor is utilised in the present study to evaluate the reliability of the mooring system under the accidental limit state. The factor is defined by the ratio of the minimum breaking load of the tendon to the maximum tension force detected under the tendon failure conditions. According to the guidance of DNVGL-OS-E301 [31], the dynamic safety factor is recommended to be no less than 1.35 for the position mooring of the FOWT system. The

safety factors calculated by the tested data, as presented in Table 10, satisfy the requirement for all the load cases, revealing that the mooring system for the present platform remains at low risk from further damage after one tendon fails.

Table 10. Maximum tension and dynamic safety factor under tendon failure conditions.

No. of tendon	Load case	Maximum tension (kN)	Dynamic safety factor
T4	LC 2	12429	1.63
	LC 5	13739	1.48
	LC 8	12824	1.58
	LC 11	13778	1.47
T5	LC 3	12588	1.61
	LC 6	11414	1.78
	LC 9	10942	1.86
	LC 12	10429	1.95

Wavelet transform is an approach of localised time-frequency analysis that applies when signals have short intervals of characteristic oscillation and short signal pieces have significance. Under the tendon failure conditions, it is insufficient to interpret the change of frequency-domain response that persists over an entire signal and ignore the transient effect that may deliver significant information by the data analysis [50]. Therefore, to further investigate the change in tendon tension under the failure conditions over time and frequency, the wavelet transform diagrams derived from the experimental results are presented in Fig. 24. As can be seen from the figures, the transient increase in tendon response frequency occurs at the moment of failure.

After the tendon fails, the energy content between 0.01 Hz to 0.15 Hz shows a significant increase, which is especially obviously seen in LC2, LC8 and LC11. The main difference between LC5 and the other three load cases is whether the wind speed was changed. Since the mean wind speed is 41 m/s, which exceeds the cut-out wind speed of the turbine, the rotor remains parked regardless of the tendon's state, while for the other three cases, the wind speed was reduced after tendon failure in the experiment to model the shutdown of the turbine. Therefore, the different result of LC5 from the other cases in the wavelet transform is likely to be related to the aerodynamic loading. To be specific, the rotation of the wind turbine can provide

aerodynamic damping to the structure, thus restraining the motion of the platform. When the aerodynamic damping, i.e. thrust force in the experiment, decreased by reducing wind speed, the motion of the platform became more drastic, which is reflected by the increase of energy content in tension force.

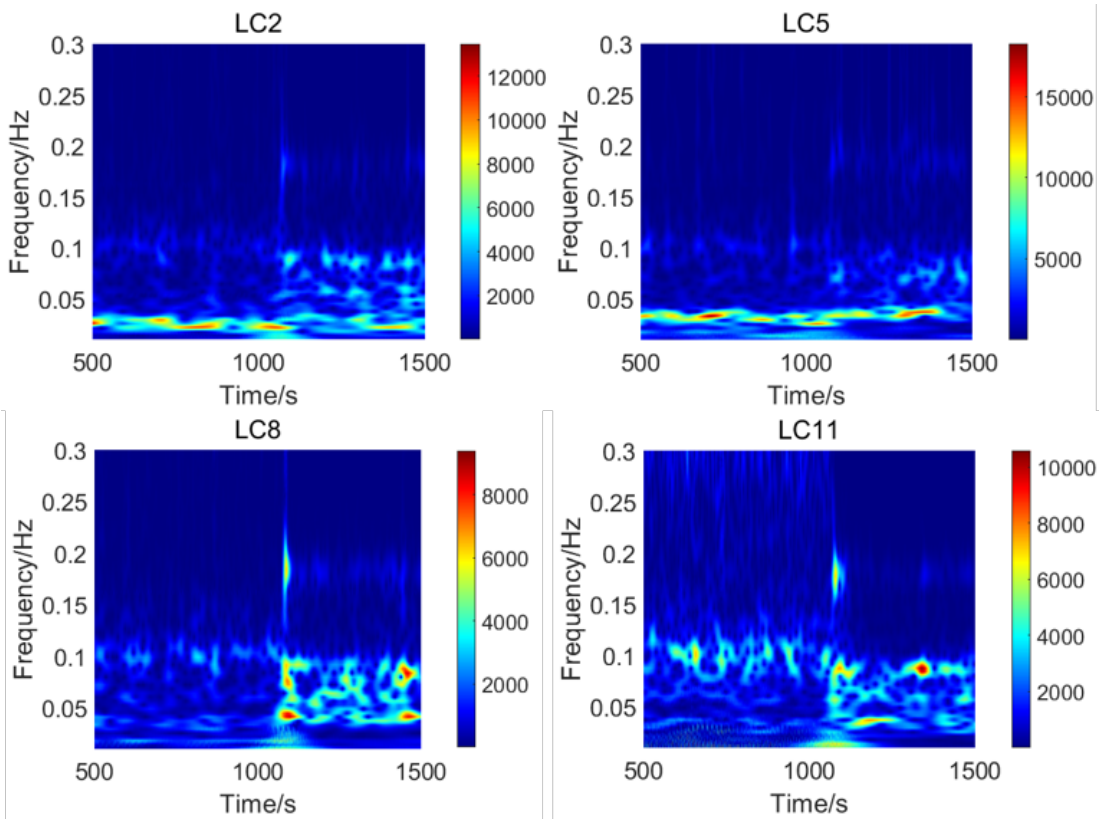

Fig. 24. Wavelet transform of tension forces in tendon T4 for LC2, LC5, LC8 and LC11.

4. Conclusions

To conclude, the dynamic analyses of a TLP FOWT supporting a 5-MW wind turbine subjected to combined wind and wave conditions were carried out using an experimental approach. The impacts of tendon failure on the platform responses and the tension forces were investigated. Some general conclusions are summarised as follows:

1) The natural periods of platform surge, heave and pitch obtained by the free-decay tests were found to be consistent with the typical range recommended by the DNV design standard.
2) The RAOs of platform's surge, heave and pitch calculated for regular wave tests illustrate the good stability of the platform under the excitation of waves.

3) The effects of tendon failure were found to be limited to the platform surge, heave and pitch response. However, the tendon adjacent to the broken tendon experienced a significant increase after the failure.
4) Among all the cases tested, the maximum tension force was found in tendon T4 (13778 kN). This is related to the lowest tendon safety factor, i.e. 1.47.
5) No slack was detected for any of the six tendons, even under the mooring failure conditions.
6) The dynamic safety factors were found to be higher than the recommended value given by the relevant standard, demonstrating the safety of the mooring system.

Acknowledgement

This research work was supported by the Institute for Energy Systems, School of Engineering at the University of Edinburgh, United Kingdom. The first author is grateful to the Royal Society of Edinburgh, for the funding provided through the John Moyes Lessells Travel Scholarship to undertake research at Dalian University of Technology, China. Also, the second author acknowledges the funding received from the National Natural Science Foundation of China (Grant No. 52071058, 51939002). This work is also partially supported by Natural Science Foundation of Liaoning Province (2022-KF-18-01) and the Fundamental Research Funds for the Central University (DUT20ZD219).

References

[1] GWEC, Global Offshore Wind Report 2022, 2022.

[2] Wang X, Zeng X, Yang X, and Li J, Feasibility study of offshore wind turbines with hybrid monopile foundation based on centrifuge modeling, Applied Energy, 2018, 209:127-139.

[3] Qin M, Shi W, Chai W, Fu X, Li L, and Li X, Extreme structural response prediction and fatigue damage evaluation for large-scale monopile offshore wind turbines subject to typhoon conditions, Renewable Energy, 2023, 208:450-464.

[4] Rinaldi G, Garcia-Teruel A, Jeffrey H, Thies P R, and Johanning L, Incorporating stochastic operation and maintenance models into the techno-economic analysis of floating offshore wind farms, Applied Energy, 2021, 301:117420.

[5] Europe W, Floating Offshore Wind Vision Statement, 2017.

[6] Gordon R B, Brown M G, and Allen E M, Mooring Integrity Management: A State-of-the-Art Review, In Proceedings of the Offshore Technology Conference, Houston, Texas, US, 2014.

[7] Cheng X, Shi F, Liu X, Zhao M, and Chen S, A Novel Deep Class-Imbalanced Semisupervised Model for Wind Turbine Blade Icing Detection, IEEE Transactions on Neural Networks and Learning Systems 2022, 33 (6):2558-2570.

[8] Zhang L, Li Y, Xu W, Gao Z, Fang L, Li R et al., Systematic analysis of performance and cost of two floating offshore wind turbines with significant interactions, Applied Energy, 2022, 321:119341.

[9] Doubrawa P, J.Churchfield M, Godvik M, and Sirnivas S, Load response of a floating wind turbine to turbulent atmospheric flow, Applied Energy, 2019, 242:1588-1599.

[10] Lozon E and Hall M, Coupled loads analysis of a novel shared-mooring floating wind farm, Applied Energy, 2023, 332:120513.

[11] Grant E, Johnson K, Damiani R, Phadnis M, and Pao L, Buoyancy can ballast control for increased power generation of a floating offshore wind turbine with a light-weight semi-submersible platform, Applied Energy, 2023, 330:120287.

[12] Gao Z, Feng X, Zhang Z-t, Liu Z, Gao X, Zhang L et al., A brief discussion on offshore wind turbine hydrodynamics problem, Journal of Hydrodynamics, 2022, 34:15-30.

[13] Zhao Z, Wang W, Shi W, and Li X, Effects of second-order hydrodynamics on an ultra-large semi-submersible floating offshore wind turbine, Structures, 2020, 28:2260-2275.

[14] Wang S and Moan T, Methodology of load effect analysis and ultimate limit state design of semi-submersible hulls of floating wind turbines: With a focus on floater column design, Marine Structures, 2024, 93:103526.

[15] Wang S, Xing Y, Balakrishna R, Shi W, and Xu X, Design, local structural stress, and global dynamic response analysis of a steel semi-submersible hull for a 10-MW floating wind turbine, Engineering Structures, 2023, 291:116474.

[16] Peng Z, Zhao H, and Li X, New ductile fracture model for fracture prediction ranging from negative to high stress triaxiality, International Journal of Plasticity, 2021, 145.

[17] Matha D, Model development and loads analysis of an offshore wind turbine on a Tnesion Leg Platform, with a comparison to other floating turbine concepts, 2009.

[18] Withee J E, Fully coupled dynamic analysis of a Floating Wind Turbine System, Doctoral Degree, Massachusetts Institute of Technology, 2004.

[19] Jonkman J M and Jr. M L B, FAST User's Guide, NREL, 2005.

[20] Ding H, Han Y, Zhang P, Le C, and Liu J, Dynamic Analysis of a New Type of Floating Platform for Offshore Wind Turbine, In Proceedings of the Twenty-sixth (2016) International Ocean and Polar Engineering Conference, Rhodes, Greece, June 26-July 1, 2016.

[21] Zhao Y, Yang J, and He Y, Preliminary Design of a Multi-Column TLP Foundation for a 5-MW Offshore Wind Turbine, Energies, 2012, 5:3874-3891.

[22] Zhao Y, She X, He Y, Yang J, Peng T, and Kou Y, Experimental Study on New Multi-Column Tension-Leg-Type Floating Wind Turbine, China Ocean Engineering, 2018, 32 (2):123-131.

[23] Naqvi S K, Scale model experiments on floating offshore wind turbines, Master of Science, Worcester Polytechnic Institute, 2012.

[24] Wright C, O'Sullivan K, Murphy J, and Pakrashi V, Experimental Comparison of

Dynamic Responses of a Tension Moored Floating Wind Turbine Platform with and without Spring Dampers, Journal of Physics: Conference Series, 2015, 628:012056.

[25] Murfet T and Abdussamie N, Loads and Reponse of a Tension Leg Platform Wind Turbine with Non-Rotating Blades: An Experiment Study, Journal of Marine Science and Engineering, 2019, 7 (56), 10.3390/jmse7030056.

[26] Oguz E, Clelland D, Day A H, Incecik A, pez J A L, anchez G S et al., Experimental and numerical analysis of a TLP floating offshore wind turbine, Ocean Engineering, 2018, 147:591-605, https://doi.org/10.1016/j.oceaneng.2017.10.052.

[27] Rega G, Nonlinear vibrations of suspended cables—Part I: Modeling and analysis, Applied Mechanics Reviews, 2004, 57 (6):443-478.

[28] Rega G, Nonlinear vibrations of suspended cables—Part II: Deterministic phenomena, Applied Mechanics Reviews, 2004, 57 (6):479-514.

[29] Ma K-T, Luo Y, Kwan T, and Wu Y, Mooring System Engineering for Offshore Structures. Elsevier Inc., 2019.

[30] DNVGL, DNVGL-RP-0286 Coupled analysis of floating wind turbines, 2019.

[31] DNVGL, DNVGL-OS-E301 Position mooring, 2015.

[32] ABS, Guidance Notes on Global Performance Analysis for Floating Offshore Wind Turbines, 2020.

[33] ABS, Guide for Position Mooring Systems, 2022.

[34] Chen X, Jiang Z, Li Q, Li Y, and Ren N, "Extended environmental contour methods for long-term extreme response analysis of offshore wind turbine," presented at the ASME Journal of Offshore Mechanics and Arctic Engineering, 2020, 052003.

[35] Cruz A and Krausmann E, Damage to Offshore Oil and Gas Facilities Following Hurricanes Katrina and Rita: An Overview, Journal of Loss Prevention in The Process Industries, 2008, 21:620-626.

[36] Whitfield S. "Lessons Learned From the Big Foot Mooring Incident." https://jpt.spe.org/lessons-learned-big-foot-mooring-incident (accessed 1 July 2021.

[37] Feng A, Chen Z, You Y, and Xing J T, Hydrodynamic Evaluation for Spar Platform Subjected to Mooring Line Failure, In Proceedings of The Twenty-second International Offshore and Polar Engineering Conference, Rhodes, Greece, 2012.

[38] O.Ahmed M, A.Yenduri, and V.J.Kurian, Evaluation of the dynamic responses of truss spar platforms for various mooring configurations with damaged lines, Ocean Engineering, 2016, 123:411-421.

[39] Cheng S, Yu Y, Yu J, Wu J, Li Z, and Huang Z, Mechanistic research on the complex motion respons of a TLP under tendon breakage, Ocean Engineering, 2021, 240 (109984).

[40] Zeng X, Shi W, Feng X, Shao Y, and Li X, Investigation of higher-harmonic wave loads and low frequency resonance response of floating offshore wind turbine under extreme wave groups, Marine Structures, 2023, 89:103401.

[41] Jia Z, Wu H, Chen H, Li W, Li X, Lian J et al., Hydrodynamic Response and Tension Leg Failure Performance Analysis of Floating Offshore Wind Turbine with Inclined Tension Legs, Energies, 2022, 15 (22):8584.

[42] Verma A, Yan J, Hu W, Jiang Z, Shi W, and Teuwen J, A review of impact loads on composite wind turbine blades: Impact threats and classification, Renewable and Sustainable Energy Reviews, 2023, 178:113261.

[43] Cai Y, Zhao H, Li X, and Liu Y, Effects of yawed inflow and blade-tower interaction on the aerodynamic and wake characteristics of a horizontal-axis wind turbine, Energy, 2023, 264:126246.

[44] Bae Y H, Kim M H, and Kim H C, Performance changes of a floating offshore wind turbine with broken mooring line, Renewable Energy, 2017, 101:364-375.

[45] Li Y, Zhu Q, Liu L, and Tang Y, Transient response of a SPAR-type floating offshore wind turbine with fractured mooring lines, Renewable Energy, 2018, 122:576-588.

[46] Wu H, Zhao Y, He Y, Shao Y, Mao W, Han Z et al., Transient response of a TLP-type floating offshore wind turbine under tendon failure conditions, Ocean Engineering, 2021, 220 (108486).

[47] Chung W C, Pestana G R, and Kim M, Structural health monitoring for TLP-FOWT (floating offshore wind turbine) tendon using sensors, Applied Ocean Research, 2021, 113:102740.

[48] Ren Y, Venugopal V, and Shi W, Dynamic Analysis of a Multi-column TLP Floating Offshore Wind Turbine with Tendon Failure Scenarios, Ocean Engineering, 2022, 245:110472.

[49] Zhang L, Shi W, Zeng Y, Michailides C, Zheng S, and Li Y, Experimental investigation on the hydrodynamic effects of heave plates used in floating offshore wind turbines, Ocean Engineering, 2023, 267:113103.

[50] Talebi S. "The Wavelet Transform." https://towardsdatascience.com/the-wavelet-transform-e9cfa85d7b34 (accessed 26th October, 2021).